

# Analysis of Tropical Cyclone Precipitation Using an Object-Based Algorithm

GREGOR SKOK

*Faculty of Mathematics and Physics, University of Ljubljana, and Centre of Excellence SPACE-SI, Ljubljana, Slovenia*

JULIO BACMEISTER AND JOSEPH TRIBBIA

*National Center for Atmospheric Research,\* Boulder, Colorado*

(Manuscript received 7 March 2012, in final form 17 August 2012)

## ABSTRACT

A recently developed object identification algorithm is applied to multisensor precipitation estimates from the Tropical Rainfall Measuring Mission (TRMM 3B42) to detect and quantify the contribution of tropical cyclone precipitation (TCP) to total precipitation between 1998 and 2008. The study period includes 1144 storms. Estimates of TCP derived here are similar in pattern and seasonal variation to earlier estimates but are somewhat higher in magnitude. Annual-mean TCP fractions of over 20% are diagnosed over large swaths of tropical ocean, with seasonal means in some regions of more than 50%. Interannual variability of TCP is examined, and a small but significant downward trend in global TCP from 1998 to 2008 is found, consistent with results from independent studies examining accumulated cyclone energy (ACE). Relationships between annual-mean ACE and TCP in each major tropical cyclone basin are examined. High correlations are found in almost every basin, although different linear relationships exist in each. The highest ACE/TCP ratios are obtained in the North Atlantic and northeast Pacific basins, with lower ratios present in the northwest Pacific and South Pacific basins.

## 1. Introduction

Precipitation associated with tropical cyclones (TCs) has only recently begun to receive attention as a metric of global TC activity (Jiang and Zipser 2010). Other measures of TC activity such as accumulated cyclone energy (ACE; Bell et al. 2000) and the power dissipation index (PDI; Emanuel 2005) are based on maximum wind speeds, and while they are likely related to other aspects of TC intensity, such as precipitation, the relationship is not yet clear. Tropical cyclone precipitation (TCP) is of interest in its own right, for its destructive potential (e.g., Villarini et al. 2011) and for its more benign role as an important component of total rainfall in many coastal regions (e.g., Englehart and Douglas 2001). Finally, TCP is a smooth, continuous, spatially integrated metric that

accounts for all potentially important aspects of TC activity: frequency, intensity, and duration as well as size, an aspect not incorporated in other measures based on peak winds or minimum pressures.

Recently global atmospheric models with resolutions of 50 km and finer have begun to capture some aspects of TC dynamics and climatology (e.g., Zhao et al. 2009). These high-resolution models simulate storm numbers and geographic distributions with reasonable success. Storm intensities, defined using maximum surface wind speeds, are not as well captured. However, diagnostics based on maximum surface wind speed may not be ideal for comparison with model simulations because peak wind is highly sensitive to resolution, in both the horizontal and the vertical. A useful step in the evaluation of tropical cyclones in global high-resolution simulations may be achieved by directly comparing TCP in observations and simulations.

Several studies have sought to quantify the contributions of TCs to precipitation in a number of critical regions around the globe (e.g., Larson et al. 2005; Ren et al. 2006; Shepherd et al. 2007). Jiang and Zipser (2010) presented the first global analysis of TCP using satellite-based precipitation measurements. Jiang and Zipser

---

\* The National Center for Atmospheric Research is sponsored by the National Science Foundation.

---

*Corresponding author address:* Gregor Skok, Faculty of Mathematics and Physics, University of Ljubljana, and Centre of Excellence SPACE-SI, Ljubljana, Slovenia.  
E-mail: gregor.skok@fmf.uni-lj.si

examined several different rainfall estimates produced by the Tropical Rainfall Measuring Mission (TRMM; Simpson et al. 1988; Huffman et al. 2007) and found general agreement in terms of fractional contribution to total rainfall from TCs. They found total TCP contributions ranging from 4% to 11% depending on basin. Their study used the Florida International University and University of Utah TRMM tropical cyclone precipitation feature (TCPF) database (Liu et al. 2008; Jiang et al. 2011) for the TRMM 2A25 analysis, and 500 km cutoff for analysis of the TRMM 3B42 data. They also tried to use the TCPF approach on the TRMM 3B42 data but found that the contiguous pixel approach that defines the extent of the TCPFs produces unrealistically large features.

The use of object-based approaches seems especially well suited to examining TCs, and in fact the notion of TCs as distinct long-lived entities has a long history. Redfield (1831) first proposed that cyclones were massive, long-lived vortices in the atmosphere. A recognition of TCs as entities with defined life cycles contributed to the development of perhaps the first systematic scientifically based hurricane forecasting by Fr. Benito Viñes, the director of the meteorological observatory of the Royal College of Belen in Havana, Cuba (e.g., Viñes 1877). More recently, object-based approaches are finding an increasing role in the study of large datasets produced by high-resolution models and by high-resolution global satellite measurements, especially in the analysis of fields with strong spatial variability such as cloud condensates and precipitation (e.g., Xu et al. 2008; Skok et al. 2009, 2010; Jiang and Zipser 2010; Bacmeister and Stephens 2011).

This study will present an independently derived object-based estimate of the contribution of TCs to global precipitation using TRMM 3B42 data collected between 1998 and 2008. We employ a modified version of the algorithm described by Skok et al. (2009). The boundaries of precipitation objects in this approach are derived entirely from the data itself. No size limits are imposed. Our results agree generally with those presented by Jiang and Zipser (2010) with similar TCP distributions in all major basins. However, our technique yields a somewhat larger global TCP over the 11-yr study period than what is obtained from the method employed by Jiang and Zipser. We also explore trends in TCP and relationships between ACE (Bell et al. 2000) and TCP. We find very high correlations between ACE and TCP in all major ocean basins, except for the northwest Pacific and northern Indian Ocean. In addition, a significant downward trend in global TCP is found over the 11 yr studied in agreement with the recent study of Maue (2011).

The paper is organized as follows: Section 2 contains a description of the datasets and analysis techniques used, including our object finding algorithm. Section 3a presents basic climatological results for TC precipitation derived from our precipitation object analysis. Section 3b discusses trends and interannual variability in TC precipitation. Relationships between TCP and the ACE diagnostic are presented in section 3c. Section 3d compares our technique for defining TC precipitation objects with other approaches. A summary and discussion is presented in section 4.

## 2. Datasets and methods

### a. TRMM 3B42 and IBTrACS

Our analysis uses two datasets. The multisensor precipitation estimate from the TRMM 3B42 (Huffman et al. 2007) is a merged product derived from a number of IR and microwave instruments on TRMM and other satellites. It is calibrated using TRMM's active precipitation radar (PR), as well as surface rain gauge data. TRMM 3B42 provided estimates of instantaneous precipitation rates every 3 h on a  $0.25^\circ \times 0.25^\circ$  grid. The dataset is restricted to tropics and midlatitudes ( $50^\circ\text{S}$ – $50^\circ\text{N}$ ) and covers the period 1998–present. In this study, we will focus on the 11-yr period between 1998 and 2008. The stability of the TRMM 3B42 data over much of this period has been examined by Dai et al. (2007).

A global database of tropical cyclone tracks extending from the mid-1800s to the present has been compiled by International Best Tracks Archive for Climate Stewardship (IBTrACS) project (Knapp et al. 2010). This track database has been endorsed by World Meteorological Organization's Tropical Cyclone Programme. The IBTrACS data contain wind speed, central pressure, center locations, and other storm properties at intervals of 6 h for all identified tropical cyclones. Uncertainties exist in best-track data. This may be especially severe in the northwest Pacific, where three independent national centers provide tracking data for TCs (e.g., Ren et al. 2011). To cross check some of our conclusions in this basin, we used the best-track data provided by Japan Meteorological Agency (JMA; <http://www.jma.go.jp/jma/jma-eng/jma-center/rsmc-hp-pub-eg/besttrack.html>).

### b. Identification of precipitation objects

We use a modified version of the method described in Skok et al. (2009, 2010) to identify objects in the TRMM 3B42 precipitation data. The algorithm uses a threshold value to delineate object boundaries. The precipitation objects themselves are 3D spatiotemporal entities (two spatial dimensions + time). Before object boundaries

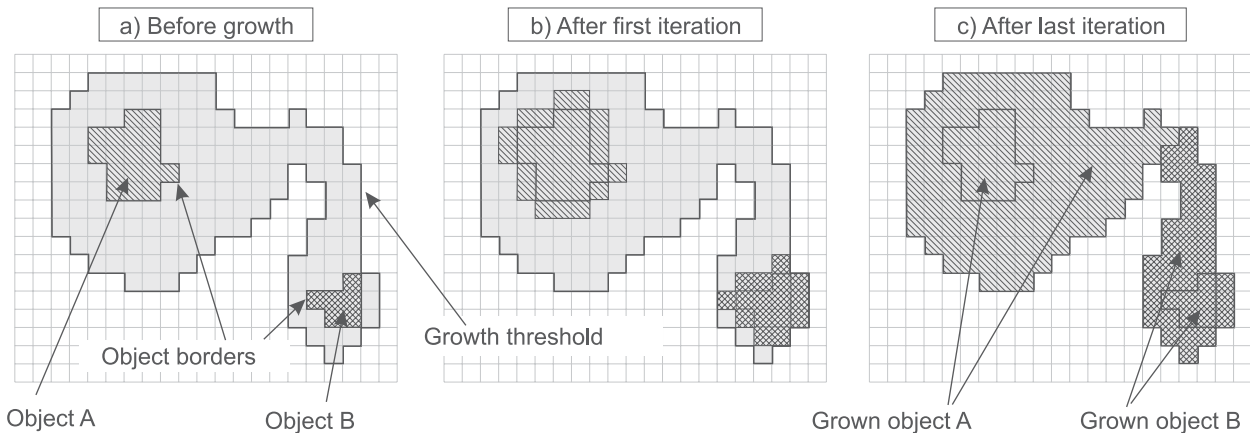


FIG. 1. Growth of objects.

are determined using a threshold value, the precipitation data are convolved with a smoothing operator in space. The technique is an extension of the Method for Object-Based Diagnostic Evaluation (MODE; Davis et al. 2006a,b, 2009) and is intended to simulate as closely as possible the object identifications made by a human observer. The choice of smoothing scales and threshold values is an important aspect of the algorithm and is discussed in detail by Skok et al. (2009, 2010). In the current study, we started with the use of the same algorithm and the same smoothing and threshold values determined to be optimal for TRMM 3B42 by Skok et al., a threshold  $T_1 = 56 \text{ mm day}^{-1}$  and a horizontal smoothing scale  $R_s = 0.75^\circ$ . However, during the course of the TC analysis we recognized that some changes were needed in the algorithm for better tracing of the TCs. Therefore, we implemented three modifications to the algorithm, which are discussed below.

### 1) GROWING OF OBJECTS

Our first modification to the object identification procedure was the introduction of concept of growing the objects (illustrated in Fig. 1). The core objects (identified by using a higher precipitation threshold) are shown by the hatched regions in Fig. 1a. A “halo” region of lower-intensity precipitation (identified by using a lower precipitation threshold) denotes the extent to which the object can be grown and is shown in Fig. 1a as a light-gray region. Next, any unclaimed pixels within the halo that are adjacent to a primary object are claimed by that object (Fig. 1b)—in this way the objects grow by one pixel in all directions provided the pixels are located inside the halo region. This process is repeated until all of the pixels within the halo have been claimed by one of the core objects (Fig. 1c).

### 2) CASCADING THRESHOLDS

The second modification was the introduction of the cascading thresholds concept. In this case a sequence of decreasing thresholds is used to distinguish distinct meteorological systems, instead of using just one threshold as was the case in Skok et al. (2009, 2010). When only a single threshold is used, if the threshold value is too high the algorithm may miss low-intensity systems and if the threshold value is too low the algorithm may merge nearby higher-intensity systems into unreasonably large single objects. In Skok et al. (2009, 2010), a thorough sensitivity analysis was performed to determine the optimal threshold value, but in the end a compromise had to be made between missing low-intensity systems and unreasonable merging of higher-intensity systems. TCs can be relatively weak systems in their starting and ending phases but very high-intensity systems in their peak phases. Moreover the TCs may contain more than one region of precipitation, with some regions being low-intensity and some being high intensity. Since we wanted to include the low- and high-intensity aspects of TCs in the analysis we introduced the concept of cascading thresholds (shown in Fig. 2). In this case a sequence of decreasing thresholds is used and the object identification is done in iterations. First the object identification is done for the highest threshold; then it is done for the next highest and so on to the lowest threshold. At each iteration, the old objects (already identified at higher thresholds) are grown to the extent determined by the current threshold while at the same time some new objects might be identified (systems with maxima smaller than the higher threshold but greater than the current threshold). Once a new object has been identified the object is not allowed to merge with other objects but is allowed to grow in each iteration by claiming “free” nearby pixels in

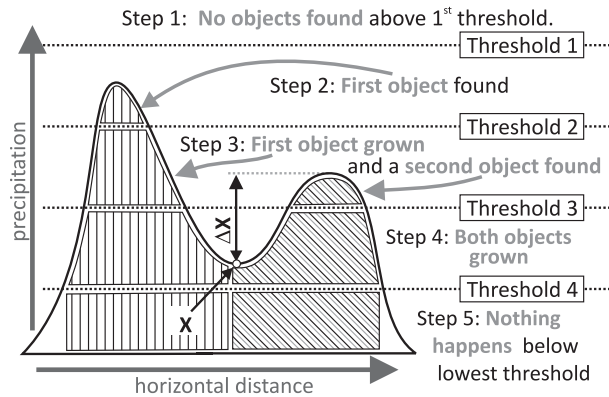


FIG. 2. An example of cascading thresholds using four threshold values.

the halo region (gray region in Fig. 1a). In this way the separate high-intensity precipitation systems are identified as separate objects while at the same time fewer low-intensity systems are missed since a relatively low minimum threshold can be used, because the danger of getting unreasonably large objects has been eliminated.

If we have a list of  $n$  cascading thresholds from  $TH_1$  to  $TH_n$ , where the difference between the thresholds is constant ( $TH_i - TH_{i-1} = \Delta TH$ ), and we have two local precipitation maxima  $X_L$  and  $X_H$  that are connected by a band of low precipitation with minimum value of  $X$  (shown with symbol  $X$  in Fig. 2), then if  $X_L \leq X_H$  and  $TH_n < X_L < TH_1 + \Delta TH$  the cascading thresholds concept guarantees that the two local maxima will be identified as separate objects if  $\Delta X > \Delta TH$ , where  $\Delta X = X_L - X$  ( $\Delta X$  is shown in Fig. 2).

The two local maxima might be identified as separate objects even if the  $\Delta X > \Delta TH$  condition is not met, but if the condition is met then the separation is guaranteed. The value  $X$  is defined as a minimum precipitation value on a chosen path between the two local maxima, where the chosen path is defined as the path that has the largest minimum precipitation value.

In Skok et al. (2009, 2010), a single threshold of  $56 \text{ mm day}^{-1}$  was used. We decided to keep this threshold but add two higher thresholds to better split the high-intensity precipitation systems into separate objects and one lower threshold to identify more of the lower-intensity systems that the  $56 \text{ mm day}^{-1}$  threshold would have missed. The four threshold values were 120, 80, 56, and  $40 \text{ mm day}^{-1}$ . The threshold values were selected in such a way to decrease by approximately 30%, thus guaranteeing identification of separate objects for precipitation features where  $\Delta X$  is more than  $\approx 30\%$  of the feature maximum precipitation. In northeast Pacific, an additional fifth threshold of  $24 \text{ mm day}^{-1}$  was used. In this region, a high number of low-intensity precipitation

systems are present that would be missed if a lowest threshold of  $40 \text{ mm day}^{-1}$  was used.

Since the lowest threshold that was used to identify objects was  $40 \text{ mm day}^{-1}$  ( $24 \text{ mm day}^{-1}$  in northeast Pacific), there were large areas of lower-intensity precipitation that were not associated with any object. This precipitation could be a significant fraction of the total precipitation. While some of this weak precipitation may in fact be unrelated to any nearby objects, we felt that much of it could be dynamically associated with more intense nearby systems (e.g., anvil rain) or growing convection at the edges of mesoscale convective complexes (MCCs).

To capture the adjacent low-intensity precipitation areas, we introduced an additional very low threshold of  $4 \text{ mm day}^{-1}$ . However, this threshold was treated differently than the higher thresholds. The objects previously defined by higher thresholds were allowed to grow as usual, but no new objects were allowed to form. Moreover, the temporal matching (the FiT concept explained in the next section) was done using objects defined by the four (or five in the northeast Pacific) higher thresholds. If the temporal matching of objects grown to  $4 \text{ mm day}^{-1}$  was allowed, the objects can merge in time because of some small overlap in the low-intensity precipitation areas.

### 3) FORWARD-IN-TIME OBJECTS

The cascading thresholds concept treats each time interval separately; there is no connection with the previous or next time interval. To study the time evolution of objects, a temporal matching of objects has to be performed after the cascading thresholds process finishes. In Skok et al., precipitation objects were simply defined as 3D objects (i.e., self-enclosed volumes) in  $x$ ,  $y$ , and  $t$  of (smoothed) precipitation above a threshold. This can lead to problems when two unrelated precipitation systems merge at some point in their lifetimes. The original 3D algorithm will identify this as a single object (Fig. 3). This is not especially worrisome when considering objects that merge soon after inception, since here retroactive identification does not necessarily lead to counterintuitive results. For example, a cluster of spatially separate convective storms could merge into a single complex over the course of several hours. A human observer may legitimately identify all of the original storms as dynamically related to the eventual longer-lived, convective complex. However, when long-lived objects merge after extensive dynamically independent evolution, a retroactive identification of the objects seems unphysical. In the present study we have modified the object identification to be “forward in time.” The forward-in-time scheme allows objects to split and retain a single identity but does not retroactively

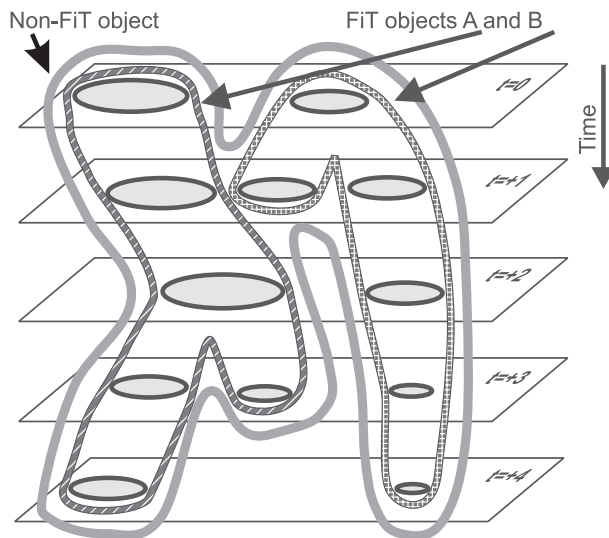


FIG. 3. Comparison of the original “fully 3D” object identification in Skok et al. (2009, 2010) and the forward-in-time object identification used here. The thick light-gray line encloses a fully 3D object containing two features that merge between  $t = +1$  and  $t = +2$ . In the original Skok et al. (2009, 2010) method, these objects, including preexisting branches and subsequent branches, are identified as a single object. In forward-in-time identification, two objects are defined for the same precipitation features (hatched dark-gray lines). The left branch of the object on the right is killed between  $t = +1$  and  $t = +2$  because it has smaller overlap area (with the object in the next time step) than the one in the left object at the time of their merger. Note that forward-in-time identification still allows objects to branch.

assign merging objects the same identity. Instead, at merger a simple check is made to determine which of the two objects has a bigger overlap area with the object in the next time step. The object with the bigger overlap area absorbs the object in the next time step and continues to exist while the one with the smaller overlap is killed (Fig. 3). The forward-in-time approach better reflects how a human would identify objects in real time and avoids misclassification of precipitation from non-TC objects as TC precipitation.

The combination of cascading thresholds and forward-in-time identification will be collectively referred to as the forward-in-time (FiT) algorithm or technique.<sup>1</sup>

<sup>1</sup> The FiT analysis software package can be obtained without charge. It can be easily compiled on Linux systems and is easy to use. Its use is not limited to precipitation; in fact, any kind of variable can be analyzed. In addition to 2D fields, it also supports full 3D fields (e.g., model variables on vertical levels). Requests to obtain the software package should be sent to the corresponding author via e-mail.

### c. TC objects identified using IBTrACS

Our initial goal was to identify TCs entirely through their signatures in the TRMM 3B42 and reanalysis data and to use the IBTrACS data as validation for this approach. However, this proved to be more difficult than we expected. Instead, for an initial characterization of TC rainfall, we adopted the compromise approach taken by Jiang and Zipser (2010) in which TC locations are taken from a TC best-track database (in our case IBTrACS) and used to classify nearby objects. TC locations from IBTrACS are linearly interpolated in time to the 3 hourly frequency of the TRMM precipitation data. We then search in a  $2.5^\circ$  ( $\approx 250$  km) radius around these TC locations for core precipitation objects: that is, those delineated by the higher threshold of  $40 \text{ mm day}^{-1}$  ( $24 \text{ mm day}^{-1}$  in northeast Pacific). If any portion of an object falls within the search radius it is identified as a potential TC. If only one object is found, then it is classified as a TC and all of its precipitation in this time interval is classified as TC precipitation. If multiple precipitation objects are found within  $2.5^\circ$  ( $\approx 250$  km) of an IBTrACS storm center, all are classified as TC objects and retain this identification forward in time as long as any part of the object (which may have more than one branch) is found inside the search radius.

### d. Definition of subregions

The global domain was separated into 16 regions or basins (Fig. 4a), which do not overlap and together cover the whole  $50^\circ\text{S}$ – $50^\circ\text{N}$  channel. The regions are either all ocean or all land, where the land–ocean distinction is determined using the European Center for Medium-Range Forecasts (ECMWF) Interim Re-Analysis (ERA-Interim) land fraction data. The ocean regions are the northeast Pacific, northwest Pacific, South Pacific, North Atlantic (also includes Mediterranean), South Atlantic, south Indian Ocean, and north Indian Ocean. The land regions are North America (includes Central America and Caribbean islands), South America, northwest Africa, southeast Africa (includes Madagascar), Southern Europe, South Asia (with Middle East), East Asia (without islands), Maritime Continent with East Asian islands (includes Japan), and Australia (includes Papua and New Zealand). The northwest Pacific region extends to the coast of the Eurasian mainland and includes the South China Sea and the Sea of Japan. TCs in the western portion of the northwest Pacific are likely to be experiencing significant interactions with land. To assess the impact of these land interactions on statistics in the northwest Pacific, we defined an “open ocean” sub-basin. The western boundary of this subbasin is shown by the dashed orange line approximately 500–1000 km to

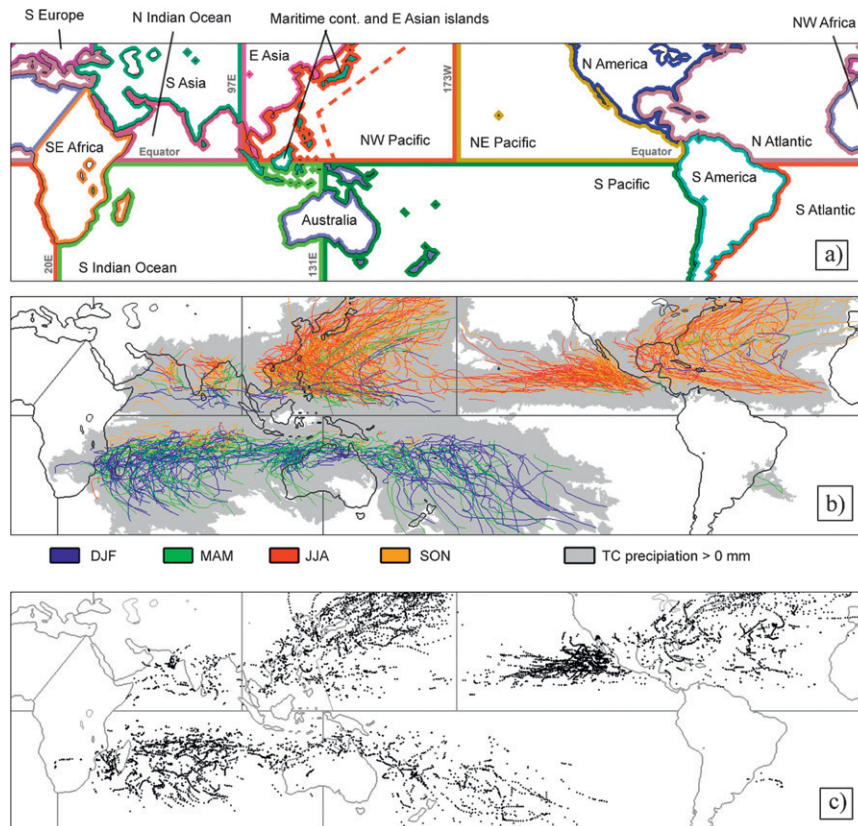


FIG. 4. (a) Definitions of domains used for analysis. Dashed orange line located east of the Philippines and Japan indicates western edge of open-ocean subbasin of northwest Pacific. (b) The TC trajectories from the IBTrACS dataset for the period 1998–2008. Colors represent seasons. Black lines represent domain borders. Light-gray shading indicates regions where any TC precipitation has been detected. (c) Locations of identified IBTrACS storm centers (1998–2008) that were not associated with any TRMM 3B42 precipitation object.

the east of the Philippines and Japan. TCs within this subbasin are unlikely to be affected by land. Figure 4b shows all IBTrACS storms for 1998–2008 color coded by season. The gray shading indicates areas where any TC precipitation was detected by the FiT algorithm during 1998–2008.

#### e. Uncertainties

The FiT algorithm provides results for TC identification and rainfall attribution that agree well with those that would be made by a human observer examining animations of TRMM 3B42 data combined with IBTrACS track information. This is a subjective assessment based on careful visual examination of extended periods of data. We have also attempted to analyze some simple quantities that would point to significant problems with the algorithm and its current tuning. One such diagnostic is the number of complete misses: that is, cases in which an IBTrACS track location is not paired with any precipitation object. Such misses occur for about 12% of

the total IBTrACS dataset. Figure 4c and Table 1 show that these misses are not uniformly distributed across basins. The largest miss rates (17%) are found in the northeast Pacific basin, where an extended dissipation phase can occur as TCs move westward over cool SSTs. The miss rate in northeast Pacific would be even larger if we did not use an additional  $24 \text{ mm day}^{-1}$  threshold in this region. Other concentrations of misses are found at the poleward of the northwest Pacific basin, in the north and central portions of the Atlantic basin, and in south Indian Basin. The net contribution to global TC precipitation from these misses is expected to be small, since they are concentrated over relatively cool SSTs.

### 3. Results

#### a. TC precipitation from 1998 to 2008

The analysis of tropical cyclone precipitation was done for an 11-yr period (1998–2008). In this period,

TABLE 1. Missed TC trajectories.

Subregion	Missed TC trajectory points	All TC trajectory points	Ratio: missed/all
Global	8123	66 608	0.12
Global sea	7462	61 464	0.12
Global land	661	5144	0.13
Northeast Pacific	1653	9468	0.17
Northwest Pacific	1753	19 361	0.09
South Pacific	891	6469	0.14
North Atlantic	958	9418	0.10
North Indian Ocean	255	2808	0.09
South Indian Ocean	1933	13 872	0.14

there were 1144 TCs in the IBTrACS dataset. The trajectories of the TCs, colored by season, can be seen in Fig. 4b. The trajectories of Northern Hemisphere (NH) and Southern Hemisphere (SH) are nicely separated by season—NH in June–August (JJA) and September–November (SON) and SH in December–February (DJF) and March–May (MAM)—although some DJF and MAM tracks can appear also in NH, mainly in the northwest Pacific and north Indian Ocean. We also see that the precipitation attributed to TCs can appear some distance away from the trajectories itself.

The annual average and seasonal averages of the daily precipitation contributed by tropical cyclones are shown in Fig. 5. It is immediately apparent that the vast majority of TC precipitation (regardless of season) falls over the oceans. The average annual precipitation has two clear local maxima, one in the northwest Pacific, east of Philippines, and one in the northeast Pacific, close to the western coast of Mexico. Other ocean regions with significant amounts of TC precipitation include the north and south Indian Ocean, the region around Australia, the northwest Atlantic, and the southwest Pacific. While the majority of TC precipitation falls over the oceans, there are numerous land regions that receive a significant amount as well. As expected, these include island and peninsular regions (e.g., Korea and Japan) as well as coastal areas. Perhaps more interesting are the significant intrusions of TC precipitation well inland during JJA and SON into eastern North America and the Indian subcontinent and during DJF and MMA into northern and western Australia.

Table 2 shows the TC precipitation volume according to different subregions and the comparison of TC precipitation to all precipitation in that region. It shows that on average the TCs contribute about 4.1% (on average  $40.6 \text{ km}^3 \text{ day}^{-1}$ ) of the global ( $50^\circ\text{S}$ – $50^\circ\text{N}$ ) precipitation. This percentage is on average higher for oceans than for land (4.8% versus 1.4%). There is also a big difference

between the NH and SH. In the NH the TCs contribute around 5.2% but only about 2.8% precipitation in the SH. As expected, the TC precipitation shifts between the NH and SH according to season: NH has more TC precipitation in JJA and SON and SH has more TC precipitation in DJF and MAM, in accordance with seasonal shift of trajectories in Fig. 4b.

Of the ocean subregions, the northwest Pacific has, by far, the maximum precipitation volume, on average around  $15.5 \text{ km}^3 \text{ day}^{-1}$ , as well as the biggest relative contribution from TCs ( $\approx 9.5\%$ ). During the peak seasons of JJA and SON, these numbers climb to around  $25 \text{ km}^3 \text{ day}^{-1}$  and 13%. After this ranked by the annual average TCP volume over the 11-yr period, the ocean basins are the south Indian Ocean ( $7.1 \text{ km}^3 \text{ day}^{-1}$ ); South Pacific ( $5.0 \text{ km}^3 \text{ day}^{-1}$ ); North Atlantic ( $4.5 \text{ km}^3 \text{ day}^{-1}$ ); northeast Pacific ( $3.5 \text{ km}^3 \text{ day}^{-1}$ ); north Indian Ocean ( $1.7 \text{ km}^3 \text{ day}^{-1}$ ); and finally South Atlantic ( $0.01 \text{ km}^3 \text{ day}^{-1}$ ), which experienced only one marginal storm during 1998–2008.

Compared to the oceans, the land subregions have much smaller TC precipitation volumes. Nevertheless, in terms of percentage, some regions get over 3% of precipitation from TCs: Australia, Maritime Continent with East Asian islands, and East Asia. In some seasons and regions TCs contribute more precipitation: that is, North America (6.9% in SON), Australia (4.6% and 5.9% in DJF and MAM), Maritime Continent with East Asian islands (5.2% and 5.3% in JJA and SON), East Asia (3.4% and 6.7% in JJA and SON), and South Asia (4.6% in SON). Some regions receive very little or almost no TC precipitation at all: that is, South America, southeast Africa, northwest Africa, and Southern Europe.

Figure 6 shows maps of seasonal and annual average TC fraction. It is striking that many coastal areas receive nearly 20% or more of their seasonal precipitation from TC, including portions of the U.S. eastern seaboard during SON. Taiwan during SON receives just over 50% of its precipitation from TCs according to our estimate. In the annual-mean large sections of ocean receive between 30% and 50% of their precipitation from TCs. Even zonal-mean TC precipitation (Fig. 7) shows annual-mean TC fractions close to 20% between  $15^\circ$  and  $20^\circ\text{N}$ . These findings are generally consistent with those of the global analysis of Jiang and Zipser (2010). Locally, the percentages are in rough agreement with earlier regional estimates. For the eastern United States, peak values close to 20% have been reported (e.g., Larson et al. 2005; Shepherd et al. 2007). Percentages of TCP close to 50% are reported for islands in the far western Pacific, including Taiwan (e.g., Kubota and Wang 2009; Chen et al. 2010).

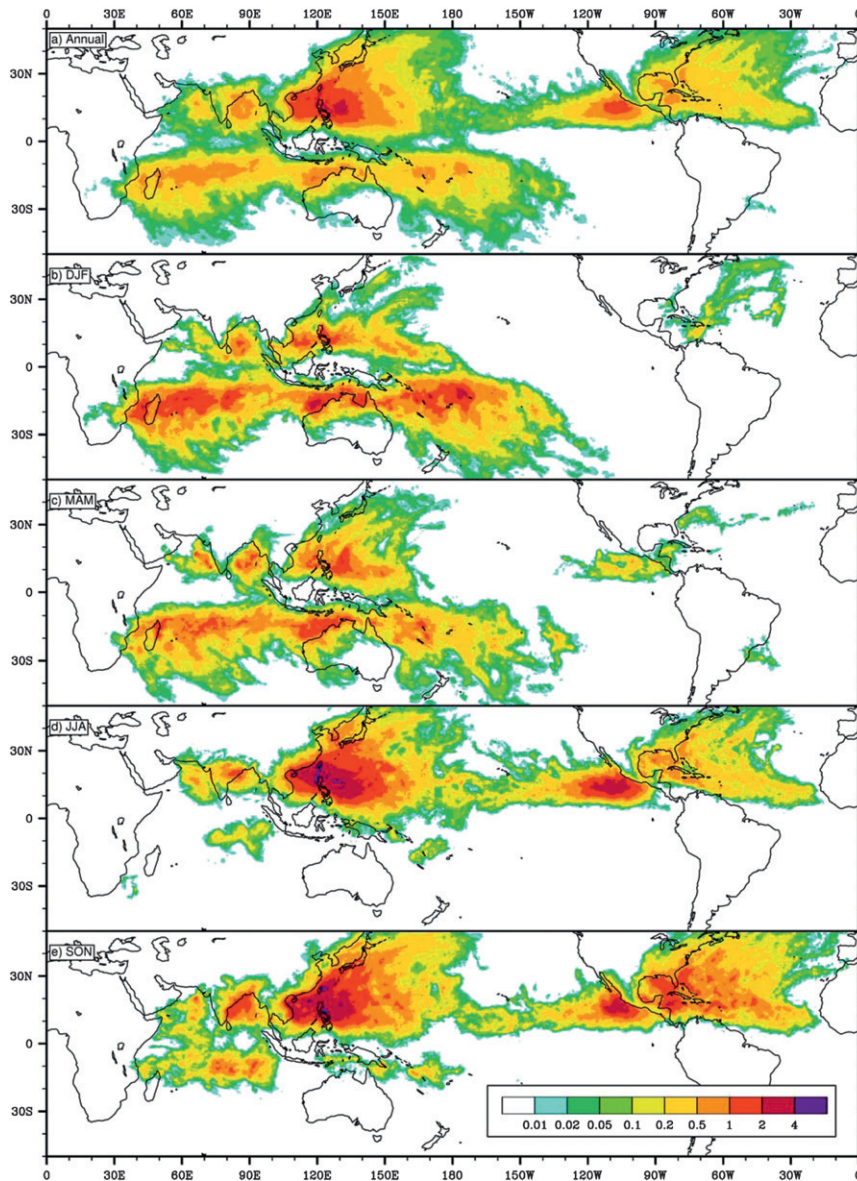


FIG. 5. Mean TC precipitation: (a) annually and (b)–(e) in each season as a function of latitude and longitude ( $\text{mm day}^{-1}$ ) for the period 1998–2008.

### b. Interannual variability

The 11-yr TRMM data record is clearly of marginal use for studying long-term climate trends in TC activity. Nevertheless, trends in TC activity over the last decade are of interest and have been remarked upon by other researchers (e.g., Maue 2011). The total TC precipitation in each year between 1998 and 2008 in our subregions is plotted in Fig. 8. There is a noticeable downward trend in the global total annual precipitation contributed by TCs. The general shape of global, NH, and SH curves in Fig. 8 is roughly similar to the ACE

(Bell et al. 2000) time series shown by Maue (2011) over the same period. The relationship between ACE and TC precipitation will be explored in more detail below. A distinct “hump” in global and NH TC precipitation is visible between 2000 and 2005. This lies on top of the general, global downward trend from 1998 to 2008. In the Southern Hemisphere there is no evidence of a rise in TC activity during 2000–05 and a relatively clear downward trend from 1998 to 2008 exists. This is again consistent with the ACE time series in Maue (2011). The 11-yr time series in the individual subregions are much noisier and few exhibit clearly identifiable trends.

TABLE 2. Average daily TC precipitation volume ( $\text{km}^3 \text{ day}^{-1}$ ) for different regions and seasons. Numbers in parentheses show the ratio between TC precipitation in the region and total precipitation in the region (%).

Subregion	TC precipitation				
	DJF	MAM	JJA	SON	Annual
Global and hemispheres					
Global	37.83 (3.74)	27.60 (2.77)	43.53 (4.25)	53.57 (5.48)	40.61 (4.05)
Global sea	35.22 (4.53)	25.72 (3.35)	39.87 (5.05)	48.70 (6.38)	37.35 (4.82)
Global land	2.61 (1.12)	1.88 (0.82)	3.67 (1.56)	4.86 (2.26)	3.26 (1.43)
NH	7.59 (1.79)	9.26 (2.13)	42.84 (6.54)	50.36 (8.30)	27.58 (5.20)
NH sea	7.17 (1.99)	8.92 (2.77)	39.20 (8.52)	45.53 (9.47)	25.26 (6.22)
NH land	0.42 (0.66)	0.34 (0.31)	3.64 (1.87)	4.82 (3.82)	2.32 (1.86)
SH	30.24 (5.15)	18.34 (3.26)	0.69 (0.19)	3.21 (0.87)	13.04 (2.76)
SH sea	28.05 (6.72)	16.80 (3.76)	0.67 (0.20)	3.17 (1.12)	12.09 (3.28)
SH land	2.19 (1.29)	1.54 (1.33)	0.03 (0.07)	0.04 (0.04)	0.95 (0.91)
Ocean subregions					
Northeast Pacific	0.00 (0.00)	0.60 (0.77)	7.94 (7.25)	5.59 (4.87)	3.54 (3.53)
Northwest Pacific	5.19 (3.85)	6.37 (4.90)	25.44 (12.58)	24.84 (13.15)	15.50 (9.45)
South Pacific	13.41 (6.16)	5.76 (2.47)	0.29 (0.17)	0.45 (0.31)	4.95 (2.56)
North Atlantic	0.47 (0.51)	0.15 (0.19)	4.83 (5.21)	12.58 (10.43)	4.51 (4.71)
South Atlantic	0.00 (0.00)	0.03 (0.06)	0.00 (0.00)	0.00 (0.00)	0.01 (0.02)
North Indian Ocean	1.51 (6.00)	1.80 (6.35)	0.99 (1.94)	2.52 (5.45)	1.71 (4.52)
South Indian Ocean	14.64 (9.79)	11.00 (7.73)	0.37 (0.35)	2.72 (2.81)	7.13 (5.78)
Land subregions					
North America	0.01 (0.09)	0.03 (0.15)	0.63 (2.07)	1.71 (6.93)	0.60 (2.63)
South America	0.00 (0.00)	0.01 (0.01)	0.00 (0.01)	0.02 (0.03)	0.01 (0.01)
Australia and Papua	1.40 (4.61)	1.07 (5.85)	0.03 (0.26)	0.03 (0.18)	0.63 (3.43)
Maritime Continent and East Asian islands	0.20 (1.22)	0.14 (0.95)	0.67 (5.23)	0.84 (5.34)	0.46 (3.14)
East Asia	0.15 (2.60)	0.10 (0.48)	1.48 (3.41)	1.36 (6.66)	0.78 (3.41)
South Asia	0.06 (0.56)	0.09 (0.53)	0.85 (2.20)	0.88 (4.56)	0.47 (2.19)
Southeast Africa	0.78 (1.63)	0.45 (1.17)	0.00 (0.00)	0.02 (0.04)	0.31 (0.82)
Northwest Africa	0.00 (0.00)	0.00 (0.00)	0.00 (0.00)	0.00 (0.03)	0.00 (0.01)
Europe	0.00 (0.00)	0.00 (0.00)	0.00 (0.00)	0.00 (0.05)	0.00 (0.02)

To examine any trends in TC precipitation more quantitatively, we regressed the time series in each study region to a linear model,

$$y(t) = a + bt + \epsilon_0(t). \quad (1)$$

Results of the regressions are shown in Table 3. The significance of the trends or slopes  $b$  was then tested by generating time series using  $a$ ,  $b$ , and  $\sqrt{\langle \epsilon_0(t)^2 \rangle}$  for each subregion. We produced 100 000 series in each subregion by adding a Gaussian distributed error  $\epsilon_i(t)$  with variance  $\sigma^2 = \langle \epsilon_0(t)^2 \rangle$  to initial series  $y(t) = a + bt$ . New linear fits were performed for each of the synthetic time series and the resulting distribution of slopes was used to estimate confidence intervals for the initial slope estimate. We see that the total global trend of  $-265 \text{ km}^3 \text{ yr}^{-2}$  is below 0 with well over 95% confidence. We also see that this negative trend is dominated by the SH contribution, and in particular by the South Pacific (Fig. 8b), which contributes  $-144 \text{ km}^3 \text{ yr}^{-2}$  of the total. In fact, of the seven individual ocean basins studied here only the South

Pacific has a trend that is below 0 with more than 95% confidence. The northeast Pacific exhibits a trend that is negative with just under 95% confidence. All other individual basins show modest negative or positive trends that are not highly significant. The overwhelmingly largest basin, the northwest Pacific, produces a nominally negative trend of  $-53 \text{ km}^3 \text{ yr}^{-2}$ , but this is embedded in a distribution that spans lower and upper confidence limits of  $b_{05\%} = -198 \text{ km}^3 \text{ yr}^{-2}$  to  $b_{95\%} = 91 \text{ km}^3 \text{ yr}^{-2}$ .

The highly significant negative trend in global TC precipitation in the presence of generally weak trends in individual ocean basins requires the existence of significant correlations or anticorrelations between basins. This will not be explored here. We also note that, if the residuals to the linear model  $\epsilon_0(t)$  are not Gaussian, the significance of the linear trends in Table 3 could also change.

Trends over land subregions are also generally weak. The exception here is South Asia (Fig. 8c), which exhibits a positive trend in TC precipitation at more than 95% confidence. The adjacent north Indian Ocean basin

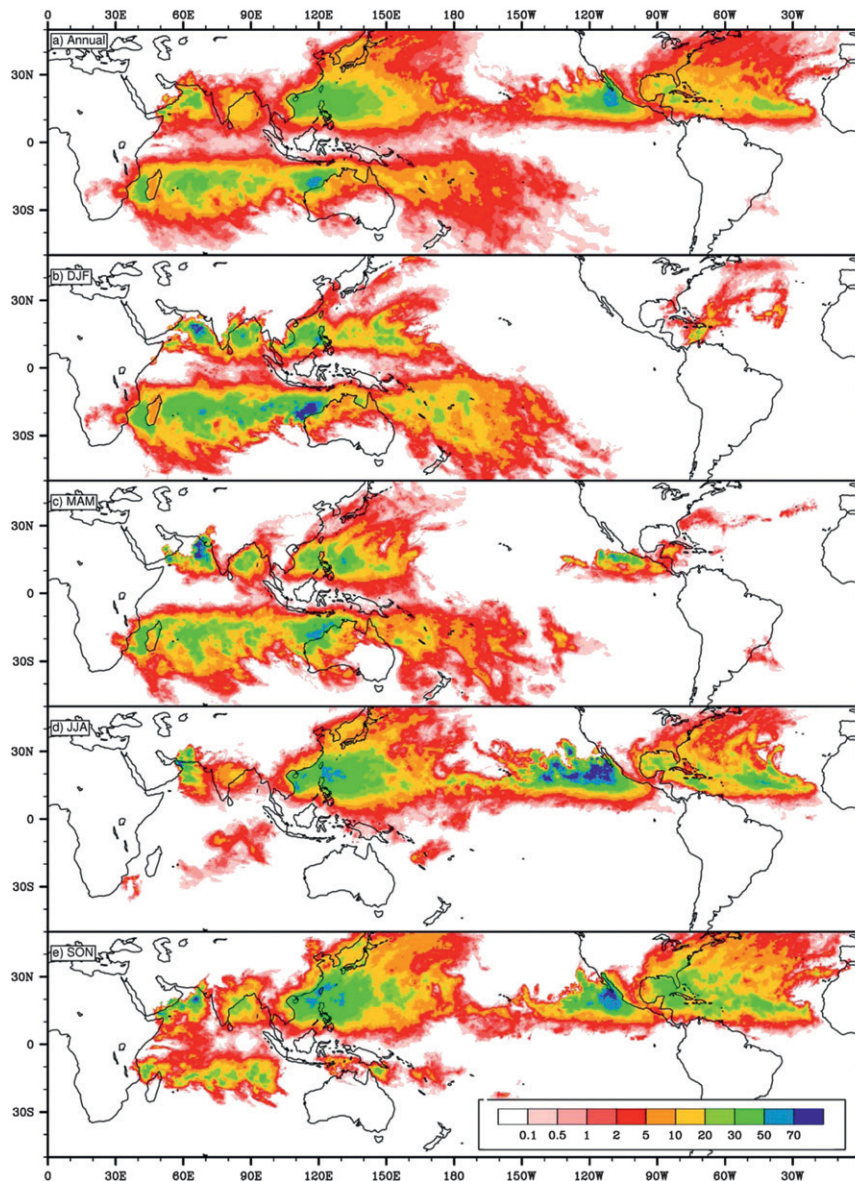


FIG. 6. Mean percentage of total precipitation contributed by TCs (a) annually and (b)–(e) in each season as a function of latitude and longitude.

(Fig. 8b) has a weakly significant positive trend. In Fig. 4 it is apparent that many storms originating in this smallest ocean basin spend a large fraction of their total life over land in the South Asia subregion. The combination of these two subregions gives a positive trend in TC precipitation at 90% confidence.

We repeat that the short 11-yr TRMM record is of marginal use in identifying long-term climate trends in TCP. Interannual variability driven by ENSO or other natural SST variability is likely to be the dominant component in any observed multiyear trend detected here. In addition, the TRMM satellite was boosted to

a higher orbit during 2001. The effects of this boost on TRMM retrievals are not yet well understood.

### c. Relationship between ACE and TC precipitation

The relationship between ACE and other measures of TC activity, including TC precipitation, is of great interest. The quantity ACE (Bell et al. 2000) is the sum of peak surface wind-based kinetic energy  $\sim V_{\max}^2$  ( $\text{kt}^2$ ) calculated over any subset of 6-hourly TC track data and divided by  $10^4$  for convenience. It has been used as an overall measure of TC activity by numerous researchers (e.g., Bell et al. 2000; Camargo and Sobel 2005; Maue

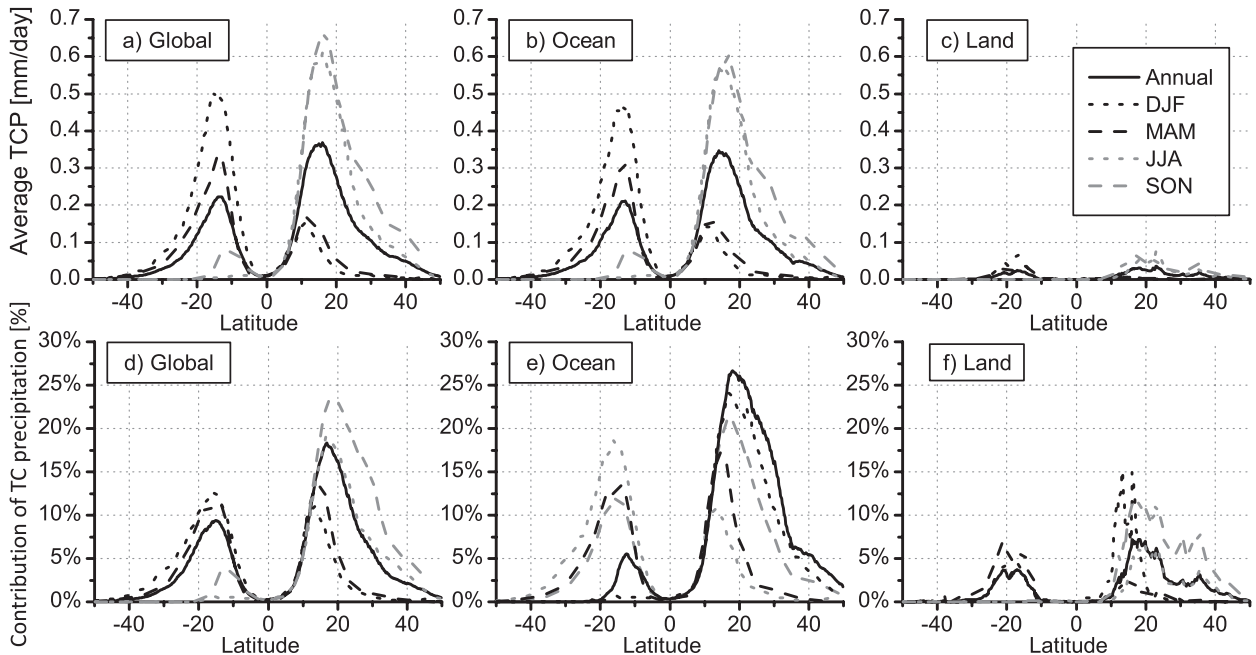


FIG. 7. Zonal profiles of (a)–(c) TC precipitation and (d)–(f) contribution of TC precipitation to all precipitation: (left) global, (middle) ocean, and (right) land.

2011). The ACE behaves in similar manner to the PDI, essentially a sum of  $V_{\max}^3$ , introduced by Emanuel (2005).

We used IBTrACS data to calculate total annual ACE for each year between 1998 and 2008 over a number of subregions. Our results for global, NH, and SH ACE (Fig. 9) agree very well with those shown in Maue (2011). As discussed earlier, the overall shape of the global, NH, and SH ACE curves and those of the corresponding TCP exhibit some rough similarities. TCP exhibits a general downward trend globally between 1998 and 2008 while ACE does not; however, they both exhibit a multiyear hump present somewhere between 2000 and 2005. The hump is more pronounced and peaks later in ACE than in TCP. In both ACE and TCP, the hump in the global mean is clearly produced by increased TC activity in the NH.

We quantify the relationship between ACE and TCP by calculating correlation coefficients between the annual time series of the two quantities and performing linear fits of ACE as a function of TCP. Table 4 shows results for several ocean subregions. The correlation between ACE and TC precipitation is over 0.8 in each major basin, except for the northwest Pacific ( $r = 0.74$ ) and the north Indian Ocean ( $r = 0.28$ ). Note that the correlation in the northwest Pacific is still significant at 90%. Figure 10 shows scatterplots of ACE versus TCP for all of the major basins. This plot, along with the best-fit ACE–TCP slopes (third column of Table 4), suggests

that different relationships between ACE and TCP exist in the basins. The South Pacific (Fig. 10, green triangles) and northwest Pacific (black crosses) basins produce storms with larger proportions of precipitation to ACE (lower ACE/TCP ratios) than the other basins. We repeated the analysis in northwest Pacific basin using JMA best-track data in place of IBTrACS (not shown) and found similar results. The highest ACE/TCP ratio occurs for storms in the northeast Pacific (blue triangles) and North Atlantic basins (red diamonds). The North Atlantic basin has the steepest slope  $b = 0.078 \times 10^{-4} \text{ kt}^2 (\text{km}^3 \text{ yr}^{-1})^{-1}$ . The south Indian Ocean (black squares) lies at intermediate ACE/TCP ratios, although the best fit slope for the basin is low [ $0.044 \times 10^{-4} \text{ kt}^2 (\text{km}^3 \text{ yr}^{-1})^{-1}$ ].

Emanuel (2006, 2007) identified significant correlations between PDI and a number of climatological variables such as SST, wind shear, and the hurricane potential intensity (PI) diagnostic (Emanuel 1986). Knutson and Tuleya (2004) found generally high correlations between peak precipitation rates and minimum central pressures in short high-resolution TC simulations. The quantity TCP is a spatially integrated quantity that may depend on aspects of TC geometry and geography that do not enter into measures of peak intensities. We speculate that the relatively low correlation in the northwest Pacific and north Indian Ocean is related to basin geography. Tracks in both basins have relatively short westward spinup phases before

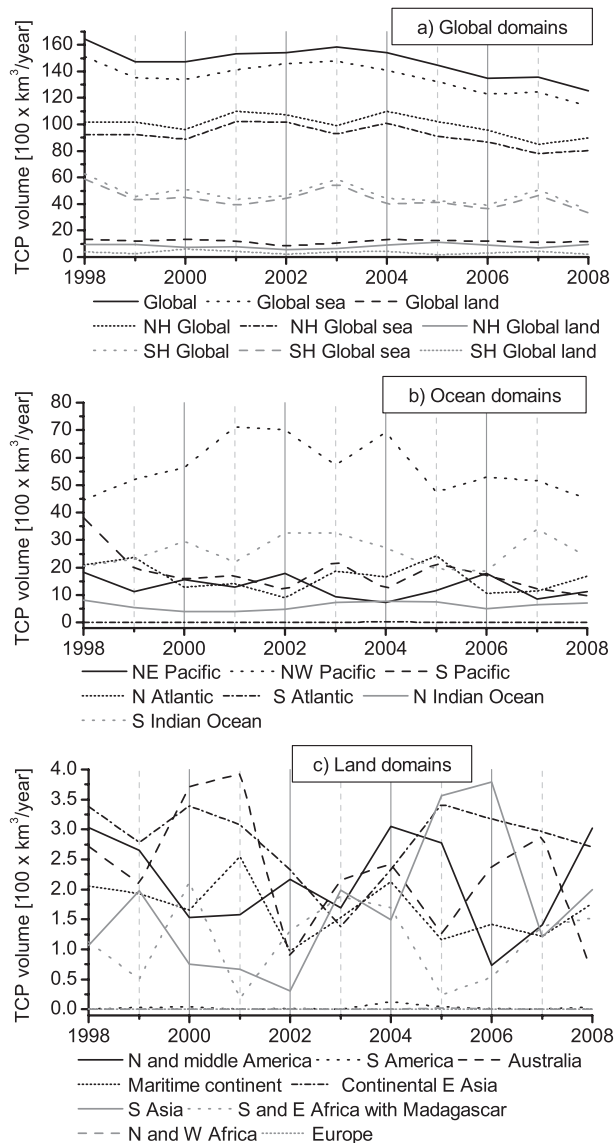


FIG. 8. Volume of TC precipitation by region for each year for 1998–2008: (a) global, (b) ocean, and (c) land domains.

recurvature or interactions with land occur, and the heaviest TC precipitation in these basins is concentrated near land areas. A subset of the storms producing this heavy precipitation could be simultaneously undergoing significant destructive interactions with land, which would reduce wind speeds (and therefore ACE) more effectively than rain rates. This process could decorrelate ACE from TCP, as well as reduce the ACE/TCP ratio in general. We tested this hypothesis in the northwest Pacific by defining an open-ocean subbasin (Fig. 4a) in which land interactions are unlikely. This subbasin has an ACE–TCP correlation of 0.93 compared with 0.74 for the whole basin (Table 4). The difference in these

correlations is significant at around 85% based on Fisher's  $z$  test. The scatterplots (Fig. 10) clearly suggest a tighter ACE–TCP relationship for the northwest Pacific open-ocean subbasin, as well as a generally higher ACE/TCP ratio.

We expect that ACE/TCP ratios are also related to storm size, with bigger storms producing more precipitation for a given peak intensity, based on wind or central pressure. Measures such as ACE and PDI account for storm frequencies and duration but not size, while TCP will clearly depend on the areal extent of heavy precipitation. Both the South Pacific and northwest Pacific have large latitudinally extensive areas of high SST ( $T > 29^\circ\text{C}$ ) during their active season [e.g., International Research Institute for Climate and Society (IRI)/Lamont-Doherty Earth Observatory (LDEO) Climate Data Library: <http://iridl.ldeo.columbia.edu>] compared to the northeast Pacific and North Atlantic basins. This may lead to a systematic difference in typical storm sizes in these basins. Note also that PI has a secondary dependence on storm size with larger radii yielding lower PI for similar environmental conditions (Emanuel 1986). Finally, TCP may depend on factors such as midlevel tropospheric humidity that are not important in determining peak intensities (e.g., Emanuel 2007).

As a check on possible uncertainty in track data we calculated ACE for the northwest Pacific basin using JMA best-track data. The differences between JMA-based and IBTrACS-based estimates of ACE were found to be small. In particular, the use of ACE based on JMA data introduced no qualitative differences in the relationship between ACE and TCP obtained using IBTrACS data (not shown).

#### d. Comparison with other attribution algorithms

The FiT algorithm was compared with other methods intended to quantify TCP. TRMM 3B42 data are used for precipitation. An important question for any method attempting to quantify TCP is whether to impose a priori restrictions on the size of the precipitation area attributed to a particular storm. Our method, FiT, attempts to avoid arbitrary size limits by using carefully chosen precipitation thresholds to define objects. Jiang and Zipser (2010) used an object-based approach with TRMM 2A25 precipitation data. Their study used the Florida International University and University of Utah TRMM TCPF database (Liu et al. 2008; Jiang et al. 2011), where objects were defined using contiguous pixels of nonzero TRMM 2A25 precipitation and any object whose unweighted geometric centroid lay within 500 km of a TC center was classed as a TCPF. The TC center locations were provided by the TC best-track database. They also

TABLE 3. Time series analysis of total TC precipitation ( $\text{km}^3 \text{yr}^{-1}$ ) during the 11-yr period 1998–2008 in each subregion considered here (Europe, northwest Africa, South Atlantic, and South America are omitted). The second column shows root-mean-square (RMS) deviations of TC precipitation in a linear model  $y = a + bt + \epsilon_0$  fitted to the TC time series shown in Fig. 7. The second column shows the linear trend  $b$  in the original time series. The next 2 columns show confidence limits on the trends. These are derived by analyzing a sequence of 100 000 (per subregion) synthetic time series  $y_i(t)$  generated by adding Gaussian noise  $\epsilon_i(t)$  with  $\sigma^2 = \langle \epsilon_0^2 \rangle$  to a time series  $y = a + bt$ . The cumulative distribution of the resulting best-fit linear slopes  $b_i$  was examined to determine the probability of slopes less than a given value. We show slope values corresponding to cumulative probability limits of 5% and 95%.

Subregion	$\sigma$ ( $\text{km}^3 \text{yr}^{-1}$ )	$b$ ( $\text{km}^3 \text{yr}^{-2}$ )	$b_{05\%}$	$b_{95\%}$
Global and hemispheres				
Global	692.2	−264.5	−373.0	−157.0
Global sea	734.9	−259.1	−374.0	−144.0
Global land	143.0	−8.6	−31.0	13.0
NH	629.0	−131.2	−230.0	−33.0
NH sea	645.1	−132.9	−234.0	−32.0
NH land	151.1	4.3	−20.0	27.0
SH	626.4	−141.2	−239.0	−44.0
SH sea	591.1	−128.5	−221.0	−36.0
SH land	114.0	−12.7	−31.0	5.0
Ocean subregions				
Northeast Pacific	347.2	−47.2	−102.0	7.0
Northwest Pacific	922.8	−53.1	−198.0	91.0
South Pacific	595.7	−144.4	−238.0	−52.0
North Atlantic	474.7	−43.5	−118.0	30.0
North Indian Ocean	142.1	10.8	−12.0	33.0
South Indian Ocean	533.5	15.4	−68.0	98.0
Land subregions				
North America	75.8	−3.8	−16.0	8.0
South America	3.4	0.1	−1.0	0.0
Australia	91.0	−13.7	−28.0	0.0
Maritime Continent and East Asian islands	40.9	−6.0	−13.0	0.0
East Asia	58.3	−2.4	−12.0	6.0
South Asia	94.5	16.0	1.0	30.0
Africa	64.2	1.2	−9.0	11.0
Combined regions				
South Asia and north Indian Ocean	185.9	26.8	−3.00	55.00

tried to use the same TCPF approach with the TRMM 3B42 dataset, which has much better temporal and spatial coverage but is of lesser quality than the radar-based 2A25. However, they discovered that the approach produced unrealistically large TCPFs in TRMM 3B42 and was not used: the problem was light rain connecting areas of more intense rain in TCs to other unrelated features. They believed the light rain in TRMM 3B42 to be spurious, caused by 3B42's low spatial resolution and overestimation of rain in cold cloud or anvil regions induced by IR observations. The precipitation feature approach has similarities with the FiT method. Both methods produce objects, and PF objects would be almost identical to the FiT objects if only one threshold of  $0 \text{ mm day}^{-1}$  were used and if objects were not matched in time. However, because of the use of nonzero cascading thresholds, the FiT method does not produce unrealistically large objects and is well suited to be used with TRMM 3B42.

Instead of using the TCPF approach, Jiang and Zipser (2010) used a simpler specified radius (SR) method with the TRMM 3B42 that defines all precipitation falling within a specified radius (500 km) of the TC center as TCP. A similar SR method was also employed by Lau and Zhou (2012). They found total contributions from TCP ranging from 4% to 11%, depending on basin.

Figure 11 shows the impact of varying the distance cutoff on TCP estimates using FiT and the SR method used by Jiang and Zipser. The SR TCP presented here was calculated for the same period as FiT and used TRMM 3B42 with IBTrACS. For ease of comparison the 500-km value of the SR method is extended to the full range of distances tried. Recall that the FiT method as used in this study employs no cutoff. The “FiT TCP” in previous sections corresponds to the value indicated by 100% on the right side of Fig. 11. From the figure we see that the radius cutoff has substantial impact on TCP estimates. For the SR method no hint of convergence is

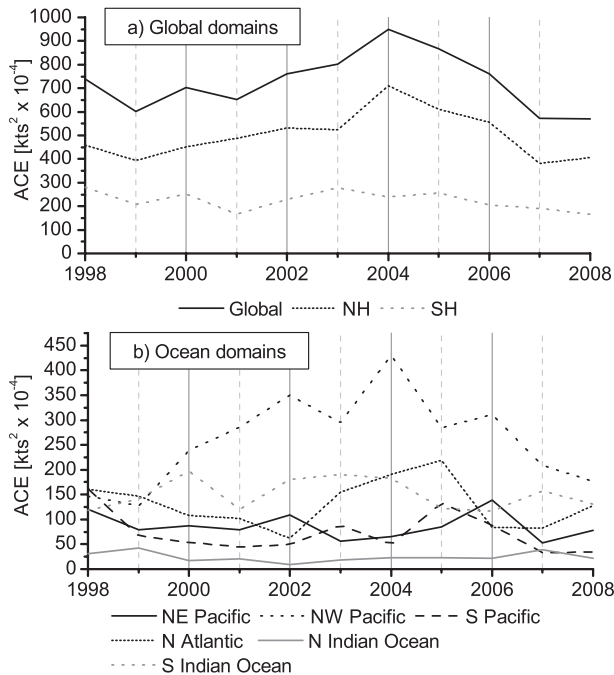


FIG. 9. ACE for each year for 1998–2008: (a) global, Northern Hemisphere, and Southern Hemisphere and (b) in each major ocean basin.

evident in the plot, and in fact TCP volume continues to increase rapidly beyond cutoff distances of 1000 km. For FiT method the increase in TCP as cutoff distances exceed 1000 km is slow, and almost no increase in TCP precipitation is present after 1500 km. With a cutoff of 500 km as used by Jiang and Zipser (2010), the SR method yields around 13% less TCP than the unrestricted FiT method.

The steepness of the SR curve around the 500-km cutoff indicates the high sensitivity of the SR method to the value of the cutoff distance. For example, increasing the cutoff distance by 50 km (from 500 to 550 km) would increase the global SR TCP by  $\approx 8\%$ . If increased to 600 km (750 km), TCP would increase by  $\approx 15\%$  ( $\approx 37\%$ ). For the SR method to give the same amount of total TCP as FiT, a cutoff distance of 597 km would have to be used. Finally, we also note that possibly spurious light rain in TRMM 3B42, caused by low spatial resolution and overestimation of rain in cold cloud or anvil regions (Jiang and Zipser 2010), might lead to overestimates of precipitation in 3B42. As a consequence, the 3B42-derived TCP might also be overestimated.

Figure 12 shows the difference between mean annual TCP derived from SR using a cutoff of 500 km (Jiang and Zipser 2010) and that derived from FiT. As expected, the differences are dominated by positive values: that is, FiT TCP is larger than that derived from the SR method. However, on the northern flank of northeast

TABLE 4. Correlation of TCP annual time series with ACE time series and slope  $b$  of linear fit assuming ACE as a function of TCP. The aggregate groups are unions of ACE–TCP points from different basins. Group 1 consists of the northwest Pacific, South Pacific, and north Indian Ocean. Group 2 consists of the North Atlantic and northeast Pacific. Correlations higher than around 0.6 are significant at 95% confidence.

Subregion	$r$	$b$ [ $10^{-4} \text{ kt}^2 (\text{km}^3 \text{ yr}^{-1})^{-1}$ ]
Global Ocean		
NH sea	0.59	0.050
SH sea	0.75	0.040
Ocean subregions		
Northeast Pacific	0.92	0.061
Northwest Pacific	0.74	0.068
South Pacific	0.90	0.047
North Atlantic	0.86	0.078
North Indian Ocean	0.28	0.014
South Indian Ocean	0.85	0.044
Aggregate groups		
Group 1	0.94	0.047
Group 2	0.88	0.077
Subbasins		
Northwest Pacific open ocean	0.93	0.061

Pacific basin FiT gives lower TCP compared with values from SR. This may not be surprising given significant number of missed TCs in the northeast Pacific (Fig. 4c), which we believe is related to the use of precipitation thresholds used in FiT. The largest absolute differences between FiT and SR occur in northwest Pacific with differences as large as  $0.5 \text{ day}^{-1}$  between FiT and SR. TCP magnitudes in northwest Pacific are also very high: up to  $2\text{--}4 \text{ mm day}^{-1}$  with broad areas between 1 and  $2 \text{ mm day}^{-1}$  (Fig. 5a). In relative terms the differences in the South Pacific appear larger. Here, FiT diagnoses broad areas of TCP between  $0.2$  and  $0.5 \text{ mm day}^{-1}$ , with differences over the same regions, with respect to SR, of the same magnitude. Interestingly, the major basin with the smallest differences, both absolute and relative, in TCP from different methods is the North Atlantic.

All the methods discussed here have possible drawbacks. The SR algorithm will not miss any precipitation within a specified distance of storm centers but could miss more extended features such as rain bands that are associated with TCs if a small cutoff distance is used. With a large cutoff, SR is likely to overestimate TC precipitation in many cases and as already said the SR TCP is very sensitive to the size of cutoff distance. The FiT algorithm does not use a specified cutoff distance and is unlikely to miss precipitation associated with strong TCs. However, it will miss weak precipitation in dissipating storms and storms over cold SSTs, as may be

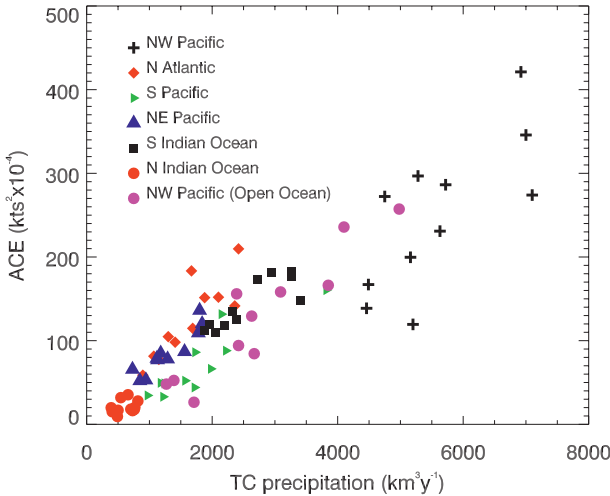


FIG. 10. ACE ( $10^{-4} \times \text{kt}^2 \text{yr}^{-1}$ ) vs TCP ( $\text{km}^3 \text{yr}^{-1}$ ) for each year 1998–2008 shown for different ocean basins in the analysis.

occurring in the northeast Pacific. This problem has been partially solved by using an additional lower threshold in the northeast Pacific.

Another problem of the FiT method might be the last step in cascading thresholds when the objects are grown to the very low threshold of  $4 \text{ mm day}^{-1}$  to capture the nearby low-precipitation areas. It could happen that the low-intensity precipitation could extend a great distance away from the TC center, thereby producing TCP far away from the TC center. To test this possibility, we limited the growth of objects to distances of 400 and 200 km. If, for example, the  $4 \text{ mm day}^{-1}$  isohyet was located closer than 400 km from the border of an object (defined by lowest threshold of 40 or  $24 \text{ mm day}^{-1}$  in the northeast Pacific), then the object was grown to the  $4 \text{ mm day}^{-1}$  isohyet as usual. If the distance to the isohyet was greater, the growth stopped 400 km (or 200 km) from the object border. The results of this analysis are shown in Fig. 11. If we impose a 400-km (200-km) limit, the total TCP is reduced by 0.4% (1.8%) compared to the

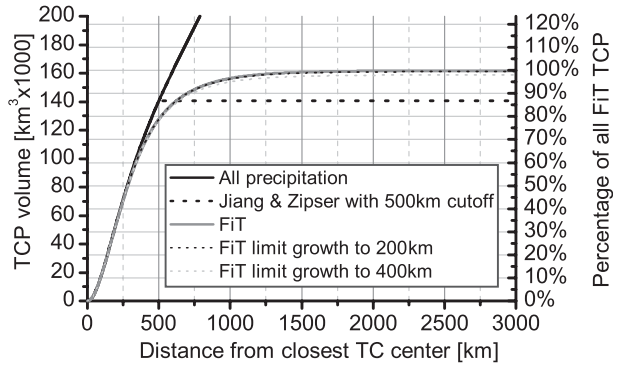


FIG. 11. Cumulative global TC precipitation volume for the period 1998–2008 as a function of cutoff distances imposed on three basic methods used to estimate TC precipitation. The most basic method simply sums all precipitation within a specified radius (SR method in the text) of a storm center.

unrestricted growth. There is some sensitivity of TCP on growth distance limit, but the effects are relatively small and we decided to use the unrestricted growth to produce all the results.

#### 4. Summary and discussion

We have presented an analysis of 11 yr from 1998 to 2008 of tropical cyclone precipitation (TCP) from a recently developed object-based analysis of TRMM 3B42 data (Skok et al. 2009) combined with track data from the IBTrACS database (Knapp et al. 2010). The precipitation object algorithm developed by Skok et al. is relatively simple but is based on statistical analysis of the underlying precipitation data itself. Arbitrary external criteria such as the 500-km radius around TC centers employed by Jiang and Zipser (2010) and Lau and Zhou (2012) to delimit TC precipitation in TRMM 3B42 are not necessary. Our results for global-mean TCP are higher by around 15% than similar TRMM 3B42–based estimates presented by Jiang and Zipser (2010). However, the overall geographical and seasonal

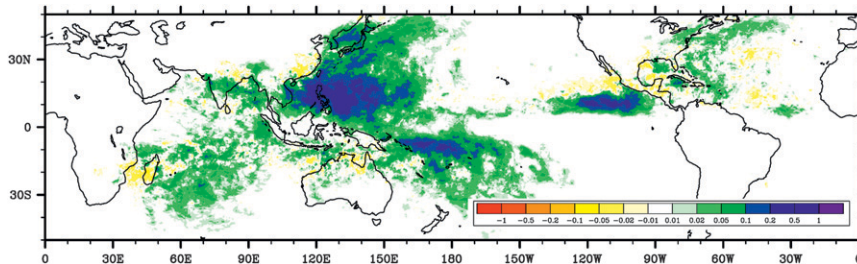


FIG. 12. Difference between annual-mean TC precipitation rates ( $\text{mm day}^{-1}$ ) calculated using FiT and the specified radius method with a cutoff radius of 500 km (Jiang and Zipser 2010) for the period 1998–2008. Positive values indicate that FiT diagnoses more TCP in a particular location.

distributions of TCP and TCP fraction are very similar to those reported in Jiang and Zipser (2010). We find seasonal fractions of over 50% in localized regions and fractions of over 20% over extensive swaths of tropical ocean even in the annual mean.

Trends in TCP were examined. We found a statistically significant downward trend (90% confidence assuming normally distributed interannual variability) in global, NH, and SH TCP over the 11 yr examined, in rough agreement with trends in ACE over the same period (Maue 2011). In the SH this downward trend came entirely from the South Pacific basin, the only individual major basin with a statistically significant downward trend (Table 3). The larger significance of these trends is not yet clear, but they are likely associated with interannual modes in tropical SSTs (e.g., Camargo and Sobel 2005; Maue 2011) rather than representing true long-term trends in TC precipitation. Interestingly, the Indian subcontinent (South Asia region) experienced a marginally significant positive trend in TCP during the same period. A small number of additional regions showed trends that appeared to verge on significance at 90% confidence: northeast Pacific (negative), Australia (negative), and combined South Asia–north Indian Ocean (positive).

It is important to relate storm precipitation to other measures of TC activity such as ACE. We examined annual-mean ACE and TCP in each major ocean basin and found distinct relationships between these two quantities (Table 4 and Fig. 10). In each basin, except for the north Indian Ocean, a statistically significant correlation was found, with  $r > 0.8$  in each basin but the northwest Pacific ( $r = 0.74$ ). However, interesting differences in the ratios of ACE to TCP appeared between the basins. Storms with heavy precipitation with respect to ACE were found in the South Pacific and northwest Pacific basin. Conversely, storms with high ACE compared to precipitation occurred in the northeast Pacific and North Atlantic basins. The south Indian Ocean exhibited an intermediate ACE/TCP ratio. A high correlation between ACE and TCP would suggest little interannual variation in the ratio of these two quantities. A possible explanation for the different ratios in the various basins could include factors such as basin geometry, with longer tracks, free of land interactions, producing higher ACE to TCP ratios. Typical storm sizes could also contribute, with geometrically large storms producing larger volumes of precipitation for given values of ACE. The ratio of ACE to TCP could be a useful diagnostic in evaluating high-resolution climate model simulations of TC activity (e.g., Zhao et al. 2009).

*Acknowledgments.* The Centre of Excellence for Space Sciences and Technologies SPACE-SI is an operation

part financed by the European Union European Regional Development Fund and the Republic of Slovenia Ministry of Education, Science, Culture and Sport.

#### REFERENCES

- Bacmeister, J., and G. Stephens, 2011: Spatial statistics of likely convective clouds in CloudSat data. *J. Geophys. Res.*, **116**, D04104, doi:10.1029/2010JD014444.
- Bell, G. D., and Coauthors, 2000: Climate assessment for 1999. *Bull. Amer. Meteor. Soc.*, **81**, s1–s50.
- Camargo, S., and A. Sobel, 2005: Western North Pacific tropical cyclone intensity and ENSO. *J. Climate*, **18**, 2996–3006.
- Chen, J., T. Li, and C. Shih, 2010: Tropical cyclone- and monsoon-induced rainfall variability in Taiwan. *J. Climate*, **23**, 4107–4120.
- Dai, A., X. Lin, and K. Hsu, 2007: The frequency, intensity, and diurnal cycle of precipitation in surface and satellite observations over low- and mid-latitudes. *Climate Dyn.*, **29** (7–8), 727–744.
- Davis, C., B. Brown, and R. Bullock, 2006a: Object-based verification of precipitation forecasts. Part I: Methodology and application to mesoscale rain areas. *Mon. Wea. Rev.*, **134**, 1772–1784.
- , —, and —, 2006b: Object-based verification of precipitation forecasts. Part II: Application to convective rain systems. *Mon. Wea. Rev.*, **134**, 1785–1795.
- , —, —, and J. Halley-Gotway, 2009: The method for object-based diagnostic evaluation (mode) applied to numerical forecasts from the 2005 NSSL/SPC spring program. *Wea. Forecasting*, **24**, 1252.
- Emanuel, K., 1986: An air–sea interaction theory for tropical cyclones. Part 1: Steady-state maintenance. *J. Atmos. Sci.*, **43**, 585–604.
- , 2005: Increasing destructiveness of tropical cyclones over the past 30 years. *Nature*, **436**, 686–688.
- , 2006: Climate and tropical cyclone activity: A new model downscaling approach. *J. Climate*, **19**, 4797–4802.
- , 2007: Environmental factors affecting tropical cyclone power dissipation. *J. Climate*, **20**, 5497–5509.
- Englehart, P., and A. Douglas, 2001: The role of eastern North Pacific tropical storms in the rainfall climatology of western Mexico. *Int. J. Climatol.*, **21**, 1357–1370.
- Huffman, G., and Coauthors, 2007: The TRMM Multisatellite Precipitation Analysis (TMPA): Quasi-global, multiyear, combined-sensor precipitation estimates at fine scales. *J. Hydrometeorol.*, **8**, 38–55.
- Jiang, H., and E. Zipser, 2010: Contribution of tropical cyclones to the global precipitation from eight seasons of TRMM data: Regional, seasonal, and interannual variations. *J. Climate*, **23**, 1526–1543.
- , C. Liu, and E. Zipser, 2011: A TRMM-based tropical cyclone cloud and precipitation feature database. *J. Appl. Meteor. Climatol.*, **50**, 1255–1274.
- Knapp, K., M. Kruk, D. Levinson, H. Diamond, and C. Neumann, 2010: The International Best Track Archive for Climate Stewardship (IBTrACS): Unifying tropical cyclone data. *Bull. Amer. Meteor. Soc.*, **91**, 363–376.
- Knutson, T., and R. Tuleya, 2004: Impact of CO<sub>2</sub>-induced warming on simulated hurricane intensity and precipitation: Sensitivity to the choice of climate model and convective parameterization. *J. Climate*, **17**, 3477–3495.

- Kubota, H., and B. Wang, 2009: How much do tropical cyclones affect seasonal and interannual rainfall variability over the western North Pacific? *J. Climate*, **22**, 5495–5510.
- Larson, J., Y. Zhou, and R. Higgins, 2005: Characteristics of land-falling tropical cyclones in the United States and Mexico: Climatology and interannual variability. *J. Climate*, **18**, 1247–1262.
- Lau, W., and Y. Zhou, 2012: Observed recent trends in tropical cyclone rainfall over the North Atlantic and the North Pacific. *J. Geophys. Res.*, **117**, D03104, doi:10.1029/2011JD016510.
- Liu, C., E. Zipser, D. Cecil, S. Nesbitt, and S. Sherwood, 2008: A cloud and precipitation feature database from nine years of TRMM observations. *J. Appl. Meteor. Climatol.*, **47**, 2712–2728.
- Maue, R., 2011: Recent historically low global tropical cyclone activity. *Geophys. Res. Lett.*, **38**, L14803, doi:10.1029/2011GL047711.
- Redfield, W. C., 1831: Remarks on the prevailing storms of the Atlantic coast of the North American states. *Amer. J. Sci. Arts*, **20**, 17–51.
- Ren, F., G. Wu, W. Dong, X. Wang, Y. Wang, W. Ai, and W. Li, 2006: Changes in tropical cyclone precipitation over China. *Geophys. Res. Lett.*, **33**, L20702, doi:10.1029/2006GL027951.
- , J. Liang, G. Wu, W. Dong, and X. Yang, 2011: Reliability analysis of climate change of tropical cyclone activity over the western North Pacific. *J. Climate*, **24**, 5887–5898.
- Shepherd, J. M., A. Grundstein, and T. L. Mote, 2007: Quantifying the contribution of tropical cyclones to extreme rainfall along the coastal southeastern United States. *Geophys. Res. Lett.*, **34**, L23810, doi:10.1029/2007GL031694.
- Simpson, J., R. Adler, and G. North, 1988: A proposed Tropical Rainfall Measuring Mission (TRMM) satellite. *Bull. Amer. Meteor. Soc.*, **69**, 278–295.
- Skok, G., J. Tribbia, J. Rakovec, and B. Brown, 2009: Object-based analysis of satellite-derived precipitation systems over the low- and midlatitude Pacific Ocean. *Mon. Wea. Rev.*, **137**, 3196–3218.
- , —, and —, 2010: Object-based analysis and verification of WRF model precipitation in the low- and mid-latitude Pacific Ocean. *Mon. Wea. Rev.*, **138**, 4561–4575.
- Villarini, G., J. A. Smith, M. L. Baeck, T. Marchok, and G. A. Vecchi, 2011: Characterization of rainfall distribution and flooding associated with U.S. landfalling tropical cyclones: Analyses of Hurricanes Frances, Ivan, and Jeanne (2004). *J. Geophys. Res.*, **116**, D23116, doi:10.1029/2011JD016175.
- Viñes, B., 1877: *Apuntes Relativos a los Huracanes de las Antillas en Septiembre y Octubre de 1875 y 76*. Nabu Press, 278 pp.
- Xu, K., T. Wong, B. Wielicki, and L. Parker, 2008: Statistical analyses of satellite cloud object data from CERES. Part IV: Boundary layer cloud objects during 1998 El Niño. *J. Climate*, **21**, 1500–1521.
- Zhao, M., I. M. Held, S.-J. Lin, and G. A. Vecchi, 2009: Simulations of global hurricane climatology, interannual variability, and response to global warming using a 50-km resolution GCM. *J. Climate*, **22**, 6653–6678.